Matter

CellPress

Article

A 4D-printed programmable soft network with fractal design and adjustable hydrophobic performance

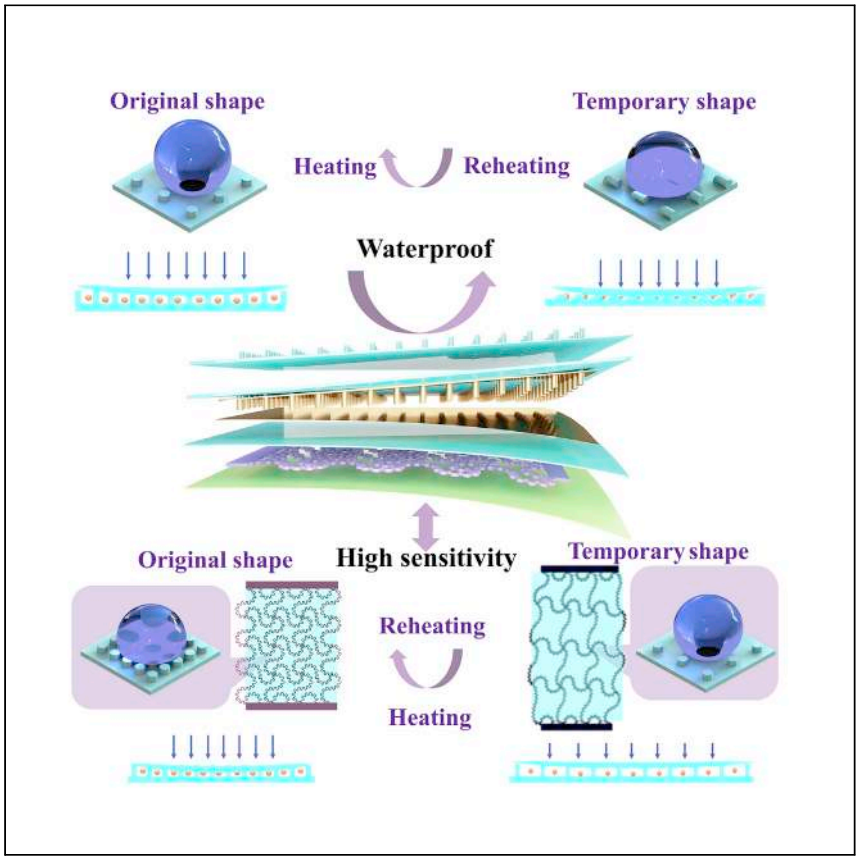

Nan Li, Wei Zhao, Fengfeng Li, Liwu Liu, Yanju Liu, Jinsong Leng

liulw@hit.edu.cn (L.L.)
lengjs@hit.edu.cn (J.L.)

Highlights

Fractal design of a 4D-printed metamaterial skeleton with biomimetic electrodes

Shape memory sensor with adjustable hydrophobic, mechanical, and electric performance

High sensitivity and flexibility of the derived health monitoring sensor

We design a fractal 4D-printed metamaterial skeleton that widens the working domain of the shape memory biomimetic sensor and enhances its adaptability and compliance with human skin. With lotus-inspired microcolumn electrodes, the novel health-monitoring sensor displays improvements in signal-to-noise ratio (SNR) and sensitivity (S). Furthermore, the sensor possesses reconfigurable properties in both mechanical and electronic functions corresponding to external stimuli. This work breaks the limitation whereby flexible sensors are pre-programmed and cannot be adjusted after fabrication. Meanwhile, it demonstrates the potential applications of 4D-printed programmable metamaterials in flexible and wearable electronics.

Improvement
Enhanced performance with innovative design or material control

Li et al., Matter 6, 1–23
March 1, 2023
https://doi.org/10.1016/j.matt.2022.12.010

Please cite this article in press as: Li et al., A 4D-printed programmable soft network with fractal design and adjustable hydrophobic performance, Matter (2022), https://doi.org/10.1016/j.matt.2022.12.010

Matter

CellPress

Article

A 4D-printed programmable soft network with fractal design and adjustable hydrophobic performance

Nan Li,[1,3] Wei Zhao,[1,3] Fengfeng Li,[1] Liwu Liu,[1,*] Yanju Liu,[1] and Jinsong Leng[2,4,*]

SUMMARY

The concept of creating novel structures by drawing inspiration from the natural world has broad prospects in bio-integrated electronics. Auxetic mechanical metamaterials have wide applications in flexible sensors, implantable medical devices, and soft robots. Here, by combining 4D-printed fractal-inspired metamaterials with microlevel biomimetic electrodes, we propose a shape memory sensor with functional and structural reconfiguration, enhanced sensitivity, and high flexibility. First, we propose the design conception and mechanical model of the 4D-printed metamaterials. Then, the metamaterial skeleton is integrated with shape memory biomimetic electrodes, which prove to possess adjustable hydrophobic and electrical performance. The derived health-monitoring sensor proves to possess reconfiguration ability in electrical and mechanical properties according to the external stimulus and high sensitivity to signal feedback with high flexibility and compliance to the human body. This work demonstrates potential applications of 4D-printed reconfigurable sensors in the fields of wearable electronics and human-computer interaction.

INTRODUCTION

After billions of years of biological evolution, many organisms, such as sharks,[1] geckos,[2,3] water striders,[4] and the lotus leaf,[5] have evolved powerful functional skins with a microstructured surface. As a representative example, the superhydrophobicity and self-cleaning ability that are found in the lotus leaf surface result from its micrometer-level columnar structure with hydrophobic epicuticular wax.[6,7] Numerous artificial materials imitating the self-cleaning and superhydrophobic structure of the lotus leaf surface have been manufactured and display application prospects in many fields.[7–10] For example, bio-inspired microhair surfaces have been utilized as an effective interfacial skin-adhesive layer of highly flexible pressure sensors with signal amplification from the microhair interfacial structures.[11] But biomimetic stimulus-responsive surfaces with programmable superhydrophobic properties that can cope with complex environmental changes remain a challenge.

Metamaterials are artificial materials whose unusual properties are derived from their periodic architecture.[12–17] As a branch of the most-studied metamaterials, auxetic metamaterials exhibit counterintuitive mechanical properties by expanding transversally when subjected to axial stretching.[18–21] Moreover, they exhibit excellent mechanical properties in terms of fracture resistance, shear resistance, variable permeability, synclastic behavior, and energy absorption.[22] However, existing auxetic metamaterials are limited in strain range and design freedom. Recent studies

PROGRESS AND POTENTIAL

The pressure signal generated by the physical contact of skin surface is an important means of perceiving tactile interaction. Therefore, flexible sensors that can convert pressure signals into electrical signals have broad application prospects in wearable electronic devices. Due to the diversity in the detected tissues, it is an ideal way to enhance sensitivity and utilization rates by fabricating sensors with reconfigurable mechanical properties to meet the needs of different target sites. Here, we propose a shape memory flexible sensor with adjustable electric and mechanical properties while maintaining high flexibility and compliance with detected sites. Ultimately, it breaks the limitation whereby the properties of sensors cannot be adjusted after fabrication. Furthermore, the sensor displays ≈ 10 and ≈ 4 times improvement in signal-to-noise ratio (SNR) and sensitivity (S), respectively, compared with flat electrodes, showing remarkable practical and scientific research prospects.

have shown that wavy chiral metamaterials provide a wide range of strain domains and a broad tunability of certain achievable mechanical properties due to their richness in lattice topology and geometry parameters. They can also achieve a biomimetic nonlinear "J-shape" curve in the stress-strain relationship.[23–27] Therefore, wavy metamaterials have immense application prospects in bio-integrated devices, soft robotics, and flexible electronics.[28–36]

Herein, inspired by 4D printing[37–41] fractal-design[42] metamaterials and biomimetic hydrophobic microstructures, we designed and fabricated a shape memory sensor[43,44] with high sensitivity, flexibility, and reconfigurability in both electrical and mechanical properties. First, we demonstrated the design conception of integrating a 4D-printed fractal-inspired metamaterial skeleton and biomimetic electrodes with lotus-inspired microcolumn array surfaces. A finite-deformation theoretical model of fractal-inspired auxetic metamaterials under uniaxial stretching was established. This serves as a guideline to optimize the mechanical properties (nonlinear strain-stress curve, Poisson's ratio, elastic modulus, etc.) of auxetic materials. Then, the mechanical properties under large deformation were investigated, and the quantitative mechanical response to strain (λ) was established. It was verified by the experimental, theoretical, and finite element analysis results that the fractal-inspired multiorder metamaterials possess reconfigurable mechanical properties while maintaining high stretchability and biomimetic J-shape mechanical curves. Therefore, the shape memory metamaterial skeleton widened the working domain of the shape memory sensor and enhanced its adaptability and compliance with human skin. Finally, with lotus-inspired microcolumn electrodes, the novel health-monitoring sensor proved to display $\approx$10 and $\approx$4 times improvement in signal-to-noise ratio (SNR) and sensitivity (S), respectively, compared with flat electrodes. Furthermore, the sensor proved to possess reconfigurable properties in both mechanical and electronic functions corresponding to external stimuli. This work breaks through the limitation whereby flexible sensors were pre-programmed in a way that cannot be adjusted after fabrication. Meanwhile, it demonstrates the potential applications of 4D-printed programmable metamaterials in flexible and wearable electronics.

RESULTS AND DISCUSSION

Conception and fabrication

A flexible sensor with high sensitivity and a large working range would have widespread applications in the health-monitoring field. However, existing work is currently limited by structural design, materials, and manufacturing methods. Herein, a highly sensitive flexible sensor combining fractal-inspired structural design and 4D-printing technology is proposed to fabricate stimulus-responsive conductive polymer composite network structures, which are expected to enhance the sensitivity and working range of strain sensors while overcoming the limitation that existing flexible sensing devices cannot adjust their properties according to the environment and application requirements after fabrication.

Figure 1A schematically illustrates the constituent parts that are integrated in the SMP (shape memory polymer)-based flexible sensor, and the detailed manufacturing process is illustrated in Figure 1B. First, a solution of D,L-polylactide (PDLLA; Jinan Daigang Biological Engineering Co., Ltd) particles and carbon tetrachloride (CCl_4) was fully stirred and defoamed (as shown in Figure 1B[I–II]), and the mixed solution was spun and coated on a silicon film to obtain microcolumn-structured interface films inspired by the superhydrophobic lotus leaf surface. At the same time, a flat slab of PDLLA film was obtained in the same way. After drying at room temperature

[1]Department of Astronautical Science and Mechanics, Harbin Institute of Technology (HIT), Harbin 150001, P.R. China

[2]Center for Composite Materials and Structures, Harbin Institute of Technology (HIT), Harbin, 150080, P.R. China

[3]These authors contributed equally

[4]Lead contact

*Correspondence: liulw@hit.edu.cn (L.L.), lengjs@hit.edu.cn (J.L.)

https://doi.org/10.1016/j.matt.2022.12.010

Please cite this article in press as: Li et al., A 4D-printed programmable soft network with fractal design and adjustable hydrophobic performance, Matter (2022), https://doi.org/10.1016/j.matt.2022.12.010

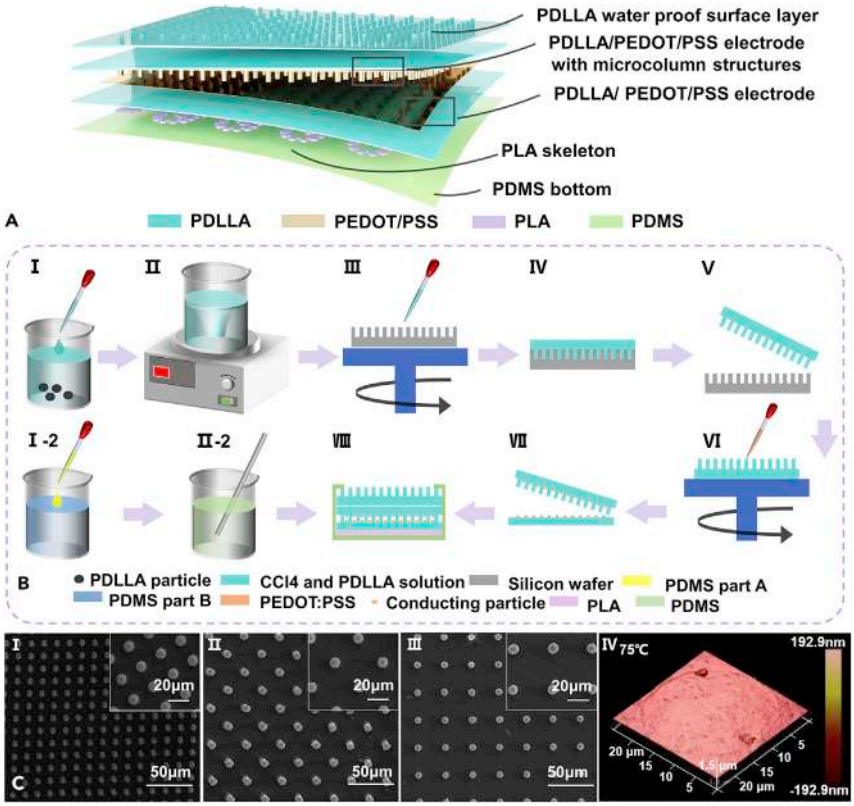

Figure 1. Schematic diagram of the constituent parts of the SMP-based flexible sensor

(A) A diagram of the constituent parts of the microlevel flexible sensor.

(B) The manufacturing process of the flexible sensor.

(C) SEM and atomic force microscopy (AFM) images of the microcolumn-structured interface membranes at 75°C.

in an aseptic environment, the films were carefully removed from the silicon film (as shown in Figure 1B[III–V]). Then a solution of 1.5% poly(3,4-ethylene dioxythiophene):poly(styrene sulfonate) (PEDOT:PSS) (Shanghai Macklin Biochemical Co., Ltd) in water was spun and coated on the positive surface of the derived films and volatilized at room temperature (as shown in Figure 1B[VI]), and the two derived conducting films (with and without microcolumn structures) were then assembled (as shown in Figure 1B[VII]) as the electrode of the capacitive sensors. Finally, a 4D-printed fractal-inspired metamaterial skeleton and a hydrophobic skin were assembled with the electrode in the way shown in Figure 1B(VIII). Here, the conducting films, as the main functional elements of the sensor, were expected to enhance the SNR of capacitive pressure sensors. The insulative microcolumn film was used as the outermost waterproof layer owing to its superhydrophobicity. And the fractal-inspired tetra-metamaterials were utilized to serve as a skeleton, intending to offer biomimetic anisotropic, nonlinear mechanical properties so that the device can be reconfigured into different configurations to adapt to different mechanical properties of detected skin tissue by the shape memory programming process. Furthermore, their negative Poisson's ratio and biomimetic J-shaped σ-λ curves were expected to improve the compliance when sticking to the skin surface and improve the sensitivity to signal feedback, Finally, polydimethylsiloxane (PDMS) was utilized as the substrate and encapsulating material to ensure high adhesion to the skin and flexibility with skin deformation. In this work, SMP-based films with microlevel cylindrical microarrays with spacings of 10, 20, and 30 μm (hereinafter referred to as

Please cite this article in press as: Li et al., A 4D-printed programmable soft network with fractal design and adjustable hydrophobic performance, Matter (2022), https://doi.org/10.1016/j.matt.2022.12.010

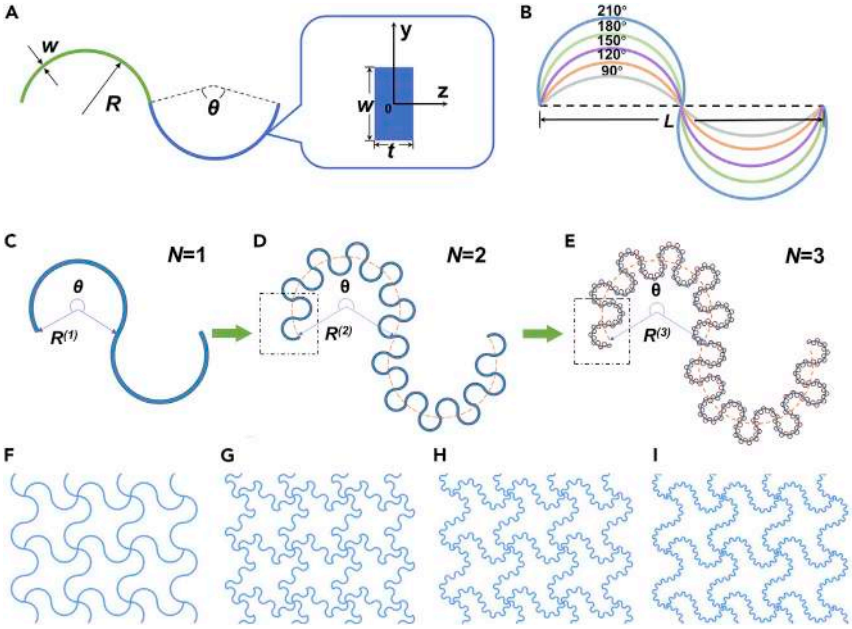

Figure 2. Schematic diagrams of the assembly process of the fractal tetra-metamaterials

(A) Control geometry parameters of the first-order and second-order filaments.

(B) First-order filaments with gradient central angle.

(C–I) The forming process of geometry composition of the fractal-inspired multiorder filaments with (C) n = 2, (D) n = 4, and (E) n = 6, and the assembled tetra units of (F) the first-order and the second-order metamaterial units with (G) n = 2, (H) n = 4, and (I) n = 6.

films I, II, and III, respectively) and a height and diameter of 10 μm were fabricated by the photolithography technology (see details in the supplemental information) as shown in Figure 1C.

The fractal-inspired metamaterial can be described as having self-similarity, where a structure is subdivided into small sections and reproduces with geometries that resemble the whole structure.[38] In this work, multiorder auxetic structures were designed. The first-order filaments consist of two centrosymmetric arcs with identical geometry parameters. The design philosophy meets the requirement when lattices are assembled topologically into overall structures as well as fissioned into multiorder microstructures according to the principle of fractal geometry. The control parameters of the first-order filaments are shown in Figure 2A, including the radius of the arc (R), width (w), radius angle (θ), and thickness (t). The span of two arcs L was set at 30 mm, and the R of the arcs and the center angle (θ = 90°, 120°, 150°, 180°, 210°) follow the geometry relationship shown in Figure 2B. The second-order filaments are fissioned by reducing the scale and connecting a certain number (2n = 2, 4, 8, 12) of first-order filaments (as shown in Figure 2C) end to end in a manner that reproduces the original geometry as the orange-dotted line shown in Figure 2D. The third-order filament is generated in the same way as illustrated in Figure 2E. $R^{(N)}$ is defined as the radii of (N)th-order microfilaments, and the relationship between $R^{(N)}$ and $R^{(N-1)}$ is given by:

$$L^i = 2R^{i-1}\sin(\theta/2n), (i = 1...N), \quad \text{(Equation 1)}$$

$$R^i = 2R^{(i-1)}\sin(\theta/2)\Big/\sin(\theta/2n), (i = 1...N). \quad \text{(Equation 2)}$$

Please cite this article in press as: Li et al., A 4D-printed programmable soft network with fractal design and adjustable hydrophobic performance, Matter (2022), https://doi.org/10.1016/j.matt.2022.12.010

The radius of the microfilaments of order (n) is related to the radii of $R^{(1)}$ by:

$$R^i = G^{(i-1)}R^{(1)}, (i = 1...N), \quad \text{(Equation 3)}$$

$$G = 2\sin(\theta/2)/\sin(\theta/2n). \quad \text{(Equation 4)}$$

Ultimately, filaments with different microstructure numbers (n = 1, 2, 4, 6) were assembled into square unit metamaterials. Here, $\overline{w}$ was set as 0.03, 0.05, 0.067, 0.083, or 0.1; gradient θ was set to vary from 0° to 210°; and the normalized thickness ($\bar{t}$) was fixed as 0.067. A set of models with the same θ = 180° is shown in Figures 2F–2I, and the fabrication process and all the specimens are shown in the supplemental information.

In this work, all the specimens were fabricated by a 3D fused deposition modeling (FDM) printer (Mega-x; Shenzhen Anycubic Technology Co., Ltd) with poly(lactic acid) filaments (PLA; Shenzhen Anycubic Technology Co., Ltd). Characterization analysis was conducted on the time- and temperature-dependent materials used in this work (see details in the supplemental information). The isothermal quasi-static uniaxial tensile tests and the stress relaxation experiments of the SMP standard specimens were conducted at gradient temperatures of 20°C, 25°C, 30°C, 40°C, 50°C, 60°C, and 70°C. It should be noted that, as the testing temperature increased from 20°C to 70°C, the SMP material underwent the glassy state, the viscoelastic state, and the highly elastic rubber state successively. Yang's modulus, the strength, and the fracture strain of the SMP specimens were 1.6 GPa, 50 MPa, and 10% at room temperature, and with the increase in environmental temperature, Yang's modulus and the strength decreased rapidly to 50 MPa and 4 MPa, with the fracture strain increasing to 10% at 70°C. The relaxation modulus test indicated that at room temperature SMP material had a higher relaxation modulus and the viscoelastic performance was not significant. But it began to show obvious viscoelasticity at 40°C, and when the material temperature reached about 60°C, the relaxation modulus of the shape memory polymer specimen decreased sharply, indicating that the material had reached the highly elastic rubber state, where the strain generated by the material could be recovered, and the maximum stress under the strain of 1.5 mm was only 0.2 MPa, while it was 38 MPa at 20°C.

In addition to the fabricated permanent shape, structures fabricated by SMP can be reconfigured with a temporary shape by the thermomechanical process after fabrication. And by applying external stimuli again, SMP structures can regain their initial permanent shape. In recent research, SMP-based materials have been utilized in the fabrication of structures with tunability and reconfigurability characteristics to realize energy absorption, mode conversion, and stimulus-response functions.

Mechanical model under infinitesimal deformation

Mechanical model of the filaments with fractal microstructures

In this subsection, the load-displacement relationship of the first-order and multiorder filaments is established (see supplemental information for details). It was assumed that the filaments only go through in-plane deformation due to the thickness (t) of the filaments being much larger than their width (w). Therefore Euler-Bernoulli beams were adopted as the deformation model of the filaments owing to their slender geometry.

First-order filaments. The Cartesian coordinate was utilized to describe the position and geometry parameters of an arbitrary filament, as Figure 3A shows, with the left

Please cite this article in press as: Li et al., A 4D-printed programmable soft network with fractal design and adjustable hydrophobic performance, Matter (2022), https://doi.org/10.1016/j.matt.2022.12.010

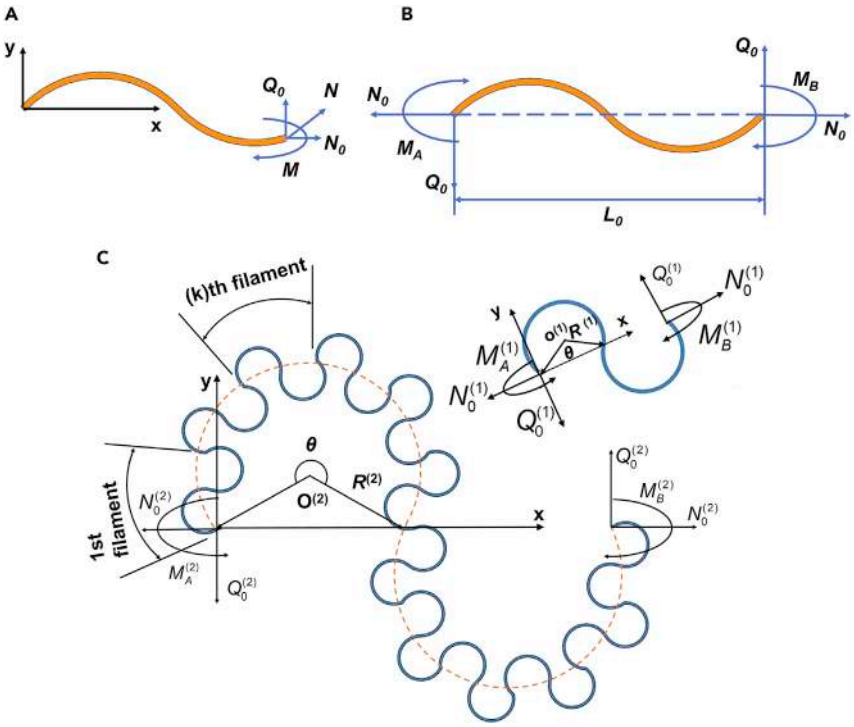

Figure 3. Graphic illustration of the first-order and the second-order filaments and their mechanical model

(A) The mechanical model of the first-order filament in the Cartesian coordinates system o-xy.

(B) The free-body mechanical illustration of the beam microstructure.

(C) The mechanical model of the second-order filament.

end of the filament set as the origin. The free-body graphic illustration of a filament is shown in Figure 3B. The total strain energy of the filament can be defined as:

$$U = 1/2E_S A\int_0^{S_0} N^2 \mathrm{dS} + 1/2E_S I\int_0^{S_0} M^2 \mathrm{dS}. \qquad \text{(Equation 5)}$$

Here, S_0 denotes the overall length of a filament, and E_S denotes the elastic modulus of the constituent material. The load-displacement equation, according to Castigliano's theorem, can be written in a dimensionless form (see details in the Mechanical Model section in the supplemental information) as:

$$\begin{Bmatrix} \overline{u} \\ \omega_A \\ \omega_B \end{Bmatrix} = \begin{bmatrix} \frac{\overline{w}^2\beta_1}{12}+\beta_5 & \frac{\overline{w}^2\beta_2}{24}+\frac{1}{2}\beta_7+\frac{1}{2}\beta_9 & -\frac{\overline{w}^2\beta_2}{24}-\frac{1}{2}\beta_9 \\ \frac{\overline{w}^2\beta_2}{24}+\frac{1}{2}\beta_7+\frac{1}{2}\beta_9 & \frac{\overline{w}^2\beta_3}{12}+\beta_4+\beta_6+\beta_8 & -\frac{\overline{w}^2\beta_3}{12}-\beta_6-\frac{1}{2}\beta_8 \\ -\frac{\overline{w}^2\beta_2}{24}-\frac{1}{2}\beta_9 & -\frac{\overline{w}^2\beta_3}{12}-\beta_6-\frac{1}{2}\beta_8 & \frac{\overline{w}^2\beta_3}{12}+\beta_6 \end{bmatrix} \begin{Bmatrix} \overline{N}_0 \\ \overline{M}_A \\ \overline{M}_B \end{Bmatrix}. \qquad \text{(Equation 6)}$$

Second-order filaments. The mechanical model of the second-order filaments is shown in Figure 3C, and the load-displacement relationship of first-order filament can be written as:

$$\begin{pmatrix} \overline{u}^{(1)} \\ \overline{w}_A^{(1)} \\ \overline{w}_B^{(1)} \end{pmatrix} = \overline{T}^{(1)} \begin{pmatrix} \overline{N}_0^{(1)} \\ \overline{M}_A^{(1)} \\ \overline{M}_B^{(1)} \end{pmatrix}, \qquad \text{(Equation 7)}$$

where

$$\left[\overline{T}^{(1)}\right] = \begin{pmatrix} \frac{1}{64}\left[\csc^3\frac{\theta}{2}(\theta+\sin\theta) - 8\cos\frac{\theta}{2}+2\cos\frac{\theta}{2}\cot\frac{\theta}{2}\right] & \frac{1}{32}\left(-\theta\cos\frac{\theta}{2}+2\csc\frac{\theta}{2}\right) & \frac{1}{32}\left(\theta\cos\frac{\theta}{2}-2\csc\frac{\theta}{2}\right) \\ \frac{1}{32}\left(-\theta\cos\frac{\theta}{2}+2\csc\frac{\theta}{2}\right) & \frac{\csc\frac{\theta}{2}}{64}\left(\theta\csc^2\frac{\theta}{2}-\csc\frac{\theta}{2}+10\theta\right) & \frac{\csc\frac{\theta}{2}}{64}\left(-\theta\csc^2\frac{\theta}{2}+\csc\frac{\theta}{2}+6\theta\right) \\ \frac{1}{32}\left(\theta\cos\frac{\theta}{2}-2\csc\frac{\theta}{2}\right) & \frac{\csc\frac{\theta}{2}}{64}\left(-\theta\csc^2\frac{\theta}{2}+\csc\frac{\theta}{2}+6\theta\right) & \frac{1}{64}\csc\frac{\theta}{2}\left(\theta\csc^2\frac{\theta}{2}-\csc\frac{\theta}{2}+10\theta\right) \end{pmatrix}. \quad \text{(Equation 8)}$$

Each second-order filament contains 2n first-order filaments. And the strain energy of a second-order filament can be written as the summary of the strain energy of the first-order microstructure contained therein:

$$W^{(2)} = \sum_{k=1}^{2n} W_k{}^{(1)} = R^{(1)} / 2EI \sum_{k=1}^{2n} \left(N_k^{(1)}R^{(1)}, M_{kA}^{(1)}, M_{kB}^{(1)}\right)\overline{T}^{(1)}\left(N_k^{(1)}R^{(1)}, M_{kA}^{(1)}, M_{kB}^{(1)}\right)^T$$

$$= R^{(1)} / 2EI\left(N_k^{(2)}R^{(2)}, M_{kA}^{(2)}, M_{kB}^{(2)}\right)\sum_{k=1}^{2n} C_k^T\overline{T}^{(1)}C_k\left(N_k^{(2)}R^{(2)}, M_{kA}^{(2)}, M_{kB}^{(2)}\right)^T. \quad \text{(Equation 9)}$$

When $1 \le k \le n$,

$$C_k = \begin{pmatrix} \cos\gamma_1/G & -\cos\gamma_1/4G\sin\gamma_3 & \cos\gamma_1/4G\sin\gamma_3 \\ -2\sin\gamma_2\sin\gamma_8+2\sin\gamma_4\sin\gamma_1 & 1+(-\cos\gamma_1\sin\gamma_4+\sin\gamma_8\cos\gamma_2)/2\sin\gamma_3 & (\cos\gamma_1\sin\gamma_4-\sin\gamma_8\cos\gamma_2)/2\sin\gamma_3 \\ -2\sin\gamma_2\sin\gamma_8 & 1+\sin\gamma_8\cos\gamma_2/2\sin\gamma_3 & -\sin\gamma_8\cos\gamma_2/2\sin\gamma_3 \end{pmatrix}. \quad \text{(Equation 10)}$$

When $n+1 \le k \le 2n$,

$$C_k = \begin{pmatrix} \frac{\cos\gamma_5}{G} & \frac{-\sin\gamma_5}{4G\sin\gamma_3} & \sin\gamma_5/4G\sin\gamma_3 \\ -2\sin\gamma_6\sin\gamma_7 & -\sin\gamma_6\cos\gamma_7/2\sin\gamma_3 & 1+\sin\gamma_6\cos\gamma_7/2\sin\gamma_3 \\ 2\sin\gamma_5\sin\gamma_4-2\sin\gamma_6\sin_7 & (\cos\gamma_5\sin\gamma_4-\sin\gamma_6\cos\gamma_7)/2\sin\gamma_3 & 1+(-\cos\gamma_5\sin\gamma_4+\cos\gamma_7\sin\gamma_6)/2\sin\gamma_3 \end{pmatrix}, \quad \text{(Equation 11)}$$

$$\gamma_1 = \theta/2n(2k-n-1), \gamma_2 = \theta/2n(n-k), \gamma_3 = \theta/2, \gamma_4 = \theta/2n,$$
$$\gamma_5 = \theta/2n(3n-2k+1), \gamma_6 = \theta/2n(2n-k+1), \gamma_7 = \theta/2n(k-n-1), \gamma_8 = k\theta/2n' \quad \text{(Equation 12)}$$

$$W^{(2)} = \frac{R^{(2)}}{2EI}\left(N^{(2)}R^{(2)}, M_A^{(2)}, M_B^{(2)}\right)\overline{T}^{(2)}\left(N^{(2)}R^{(2)}, M_A^{(2)}, M_B^{(2)}\right)^T. \quad \text{(Equation 13)}$$

The second-order elastic flexibility matrix $\overline{T}^{(2)}$ is defined as:

$$\overline{T}^{(2)} = G\sum_{k=1}^{2n} C_k^T\overline{T}^{(1)}C_k. \quad \text{(Equation 14)}$$

The transition matrix [*D*] depends only on θ and n, and the matrix elements can be obtained from:

$$\left(\overline{T}_{11}^{(2)}, \overline{T}_{22}^{(2)}, \overline{T}_{33}^{(2)}, \overline{T}_{12}^{(2)}, \overline{T}_{13}^{(2)}, \overline{T}_{23}^{(2)}\right)^T = D\left(\overline{T}_{11}^{(1)}, \overline{T}_{22}^{(1)}, \overline{T}_{33}^{(1)}, \overline{T}_{12}^{(1)}, \overline{T}_{13}^{(1)}, \overline{T}_{23}^{(1)}\right)^T, \quad \text{(Equation 15)}$$

$$\left(\overline{T}_{11}^{(n)}, \overline{T}_{22}^{(n)}, \overline{T}_{33}^{(n)}, \overline{T}_{12}^{(n)}, \overline{T}_{13}^{(n)}, \overline{T}_{23}^{(n)}\right)^T = D^{n-1}\left(\overline{T}_{11}^{(1)}, \overline{T}_{22}^{(1)}, \overline{T}_{33}^{(1)}, \overline{T}_{12}^{(1)}, \overline{T}_{13}^{(1)}, \overline{T}_{23}^{(1)}\right)^T, \quad \text{(Equation 16)}$$

Please cite this article in press as: Li et al., A 4D-printed programmable soft network with fractal design and adjustable hydrophobic performance, Matter (2022), https://doi.org/10.1016/j.matt.2022.12.010

$$\left(\overline{T}_{11}^{(2)}, \overline{T}_{22}^{(2)}, \overline{T}_{33}^{(2)}, \overline{T}_{12}^{(2)}, \overline{T}_{13}^{(2)}, \overline{T}_{23}^{(2)}\right)^T = \left(\lim_{m \to +\infty} D^{n-1}\right)\left(\overline{T}_{11}^{(1)}, \overline{T}_{22}^{(1)}, \overline{T}_{33}^{(1)}, \overline{T}_{12}^{(1)}, \overline{T}_{13}^{(1)}, \overline{T}_{23}^{(1)}\right)^T,$$

(Equation 17)

$$[D] = \begin{pmatrix} c_{11}^2 & c_{21}^2 & c_{31}^2 & 2c_{11}c_{21} & 2c_{11}c_{31} & 2c_{21}c_{31} \\ c_{12}^2 & c_{22}^2 & c_{32}^2 & 2c_{12}c_{22} & 2c_{12}c_{32} & 2c_{32}c_{22} \\ c_{13}^2 & c_{23}^2 & c_{33}^2 & 2c_{13}c_{23} & 2c_{13}c_{33} & 2c_{23}c_{33} \\ c_{11}c_{12} & c_{12}c_{21} & c_{31}c_{32} & c_{21}(c_{12}+c_{22}) & c_{12}c_{31}+c_{11}c_{32} & c_{22}c_{31}+c_{21}c_{32} \\ c_{11}c_{13} & c_{21}c_{23} & c_{31}c_{33} & c_{21}c_{31}+c_{11}c_{23} & c_{13}c_{31}+c_{11}c_{33} & c_{23}c_{31}+c_{21}c_{33} \\ c_{12}c_{13} & c_{22}c_{23} & c_{32}c_{33} & c_{13}c_{22}+c_{12}c_{23} & c_{13}c_{31}+c_{12}c_{33} & c_{22}c_{32}+c_{23}^2 \end{pmatrix}$$

.(Equation 18)

Mechanical model of the tetra-metamaterial

Here, only the representative unit needs to be analyzed, due to the periodicity of the microstructures. And to establish the mechanical response model of the fractal-inspired auxetic metamaterials, the static equilibrium equation and deformation compatibility equation were combined with the load-displacement equation derived above. Furthermore, the auxetic structure exhibited mechanical anisotropy results from the 4-fold rotational symmetry, and therefore, two representative directions, 0° and 45°, were chosen to be analyzed.

The tetra-metamaterial is subjected to uniaxial stretching along the vertical direction (0°), as Figure 4A illustrates, and the representative unit cell consisting of four filaments is shown in Figure 4B. The stress analysis is shown in Figure 4C; where four different filaments are indexed as 1, 2, 3, and 4, let N_i, M_{iA}, M_{iB}, and Q_i (i = 1, 2, 3, 4) indicate the axial force, bending moments, and shear force of each filament. The equilibrium condition of the internal node of the representative unit is:

$$\overline{N}_1 + \overline{N}_3 = 0, \quad \text{(Equation 19a)}$$

$$(\overline{M}_{2A} - \overline{M}_{2B}) + (\overline{M}_{4A} - \overline{M}_{4B}) = 0, \quad \text{(Equation 19b)}$$

$$(\overline{M}_{1A} - \overline{M}_{1B}) + (\overline{M}_{3A} - \overline{M}_{3B}) = 0, \quad \text{(Equation 19c)}$$

$$\overline{N}_2 - \overline{N}_4 + (\overline{M}_{1A} - \overline{M}_{1B}) - (\overline{M}_{3A} - \overline{M}_{3B}) = 0, \quad \text{(Equation 19d)}$$

$$(\overline{M}_{2A} - \overline{M}_{2B}) - \overline{N}_1 - (\overline{M}_{4A} - \overline{M}_{4B}) + \overline{N}_3 = 0, \quad \text{(Equation 19e)}$$

$$\overline{M}_{1B} + \overline{M}_{2B} + \overline{M}_{3B} + \overline{M}_{4B} = 0, \quad \text{(Equation 19f)}$$

$$\sigma_y = (\overline{N}_1 + \overline{N}_3) / \left[4tL_0\left(L_0^2 / E_s I\right)\right]. \quad \text{(Equation 19g)}$$

Then the deformation compatibility (as shown in Figure 4E) under infinitesimal deformations gives the deformation coordination relationship between the deformation components as:

$$\omega_{2A} = \omega_{4A}, \quad \text{(Equation 20a)}$$

$$\omega_{1A} = \omega_{3A}, \quad \text{(Equation 20b)}$$

$$\text{with } \omega_{iA} + \omega_{iB} = C\ (i = 1, 2, 3, 4). \quad \text{(Equation 20c)}$$

Please cite this article in press as: Li et al., A 4D-printed programmable soft network with fractal design and adjustable hydrophobic performance, Matter (2022), https://doi.org/10.1016/j.matt.2022.12.010

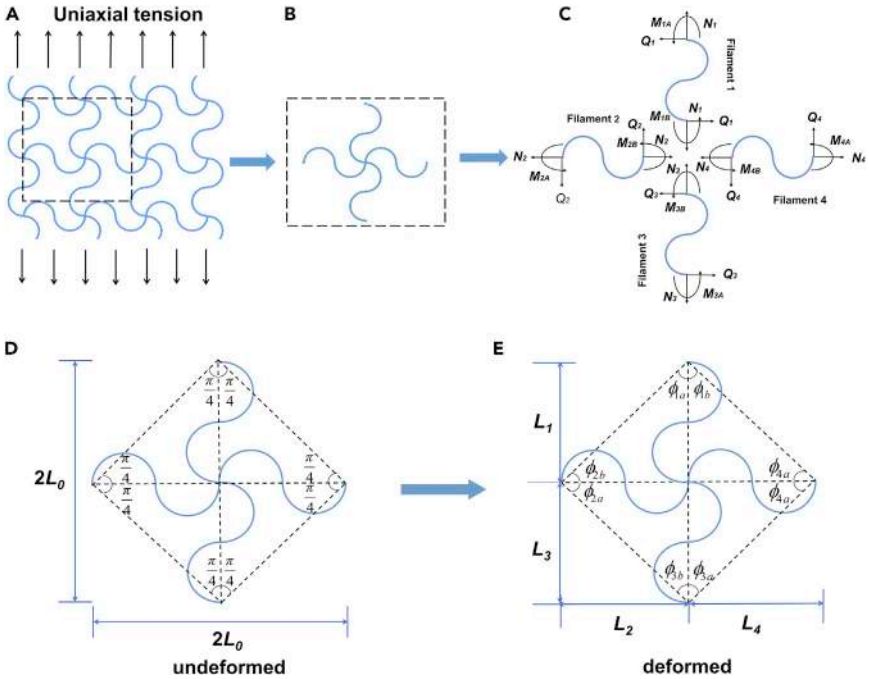

Figure 4. Schematic diagrams of the mechanic and deformation models of the representative unit of the auxetic metamaterial

(A) A tetra auxetic metamaterial that is subjected to uniaxial tensile stress along the perpendicular direction.

(B) A representative unit of the tetra auxetic metamaterial.

(C) The free-body diagram of four filaments in a representative unit.

(D) An undeformed representative unit.

(E) A deformed representative unit.

The effective strain is defined as the elongation percentage:

$$\varepsilon_y = (\overline{u}_1 + \overline{u}_3)/2, \quad \text{(Equation 21)}$$

and the load-displacement relationship of the four filaments in a representative unit in dimensionless form can be defined as the following equation with the matrix $[T]$ related to β_i (i = 1 … 8) (see details in the supplemental information):

$$\begin{bmatrix} \overline{u}_1 & \overline{u}_2 & \overline{u}_3 & \overline{u}_4 \\ \omega_{1A} & \omega_{2A} & \omega_{3A} & \omega_{4A} \\ \omega_{1B} & \omega_{2B} & \omega_{3B} & \omega_{4B} \end{bmatrix} = \begin{bmatrix} t_{11} & t_{12} & t_{13} \\ t_{12} & t_{22} & t_{23} \\ t_{13} & t_{23} & t_{33} \end{bmatrix} \begin{bmatrix} \overline{N}_1 & \overline{N}_2 & \overline{N}_3 & \overline{N}_4 \\ \overline{M}_{1A} & \overline{M}_{2A} & \overline{M}_{3A} & \overline{M}_{4A} \\ \overline{M}_{1B} & \overline{M}_{2B} & \overline{M}_{3B} & \overline{M}_{4B} \end{bmatrix}. \quad \text{(Equation 22)}$$

According to the geometry relation of network metamaterial, the analytical solution to elastic modulus (E) and Poisson's ratio (v) of the fractal tetra-metamaterial is given as:

$$E = \frac{\sigma_x}{\varepsilon_x} = -\frac{(t_{22}+2t_{23}+t_{33})E_s\overline{w}^3}{12\sqrt{2}\left(t_{12}^2+2t_{12}t_{13}+t_{13}^2-2t_{11}t_{22}-4t_{11}t_{23}-2t_{11}t_{33}\right)}, \quad \text{(Equation 23)}$$

$$v = -\frac{\varepsilon_y}{\varepsilon_x} = \frac{(t_{12}+t_{13})^2}{t_{12}^2+2t_{12}t_{13}+t_{13}^2-2t_{11}t_{22}-4t_{11}t_{23}-2t_{11}t_{33}}. \quad \text{(Equation 24)}$$

Similarly, the E and v of the tetra-metamaterial in the diagonal direction are written as:

Please cite this article in press as: Li et al., A 4D-printed programmable soft network with fractal design and adjustable hydrophobic performance, Matter (2022), https://doi.org/10.1016/j.matt.2022.12.010

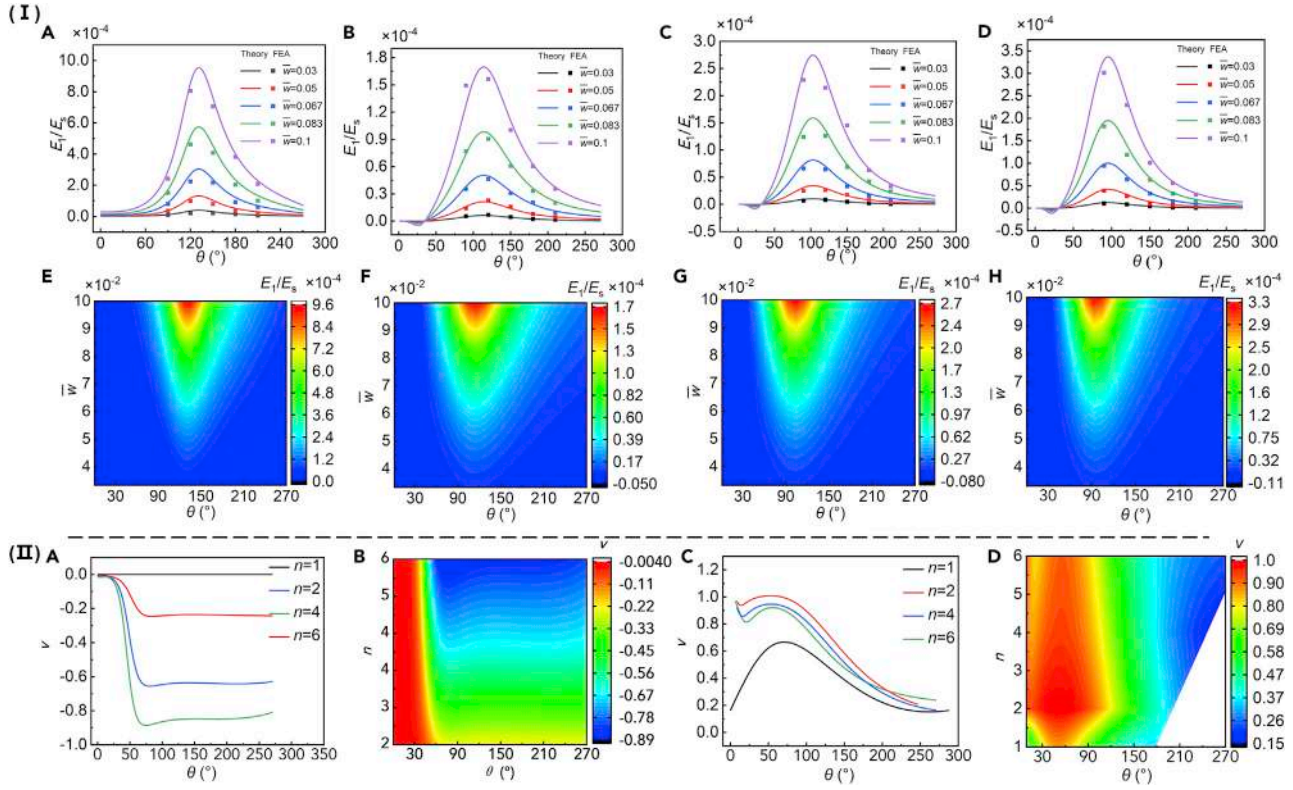

Figure 5. Theory and FEA results of the influence of geometric parameters on the elastic modulus and Poisson's ratio of the fractal-inspired metamaterials

(I) Theory and FEA results of the influence of geometric parameters on the elastic modulus in the 0° direction of the fractal metamaterials under infinitesimal deformation: (A and E) the first-order metamaterials and (B–D) and (F–H) the second-order metamaterials with n = 2, 4, 6.

(II) Theoretical results of the impacts of geometric parameters of filaments on Poisson's ratio under infinitesimal deformation: theoretical and FEA results of the influence of geometric parameters on the elastic modulus of second-order fractal-inspired metamaterials under infinitesimal deformation in the (A and B) 0° and (C and D) 45° directions.

$$E_{diagonal} = \frac{(t_{22}+2t_{23}+t_{33})E_s\overline{w}^3}{6\left[2t_{11}(t_{22}+2t_{23}+t_{33})+t_{12}(t_{22}+t_{23})+t_{13}(t_{22}+t_{23})+2t_{22}t_{33}-2t_{23}^2\right]}, \quad \text{(Equation 25)}$$

$$\nu_{diagonal} = -\frac{2t_{11}(t_{22}+2t_{23}+t_{33})+t_{12}(t_{22}+3t_{23}+2t_{33})-t_{13}(t_{22}+t_{23})-2t_{22}t_{33}+2t_{23}^2}{2t_{11}(t_{22}+2t_{23}+t_{33})+t_{12}(t_{22}+t_{23})+t_{13}(t_{22}+t_{23})+2t_{22}t_{33}-2t_{23}^2}. \quad \text{(Equation 26)}$$

Figure 5I represents the finite element analysis (FEA) and theoretical results curves and contour plots of the equivalent elastic modulus (E_1/E_s) of the fractal-inspired auxetic metamaterials under infinitesimal deformation in the 0° direction, which is related to θ, N, and n. The FEA was executed by utilizing beam elements with the same boundary conditions as the theoretical model. The theory model predictions are in perfect agreement with FEA results for all configurations. Figures 5I(A) and 5I(E) respectively exhibit curve graphs and contour plots to illustrate the impacts of the first-order metamaterials in the 0° direction. The results showed that E_1/E_s first increased with θ increase from 0 and reached their maximum values when θ equaled 130° and then decreased with the increase in θ. This was because at 130°, the microstructure at both ends of the filament in the vertical direction was perpendicular to the vertical direction, and the two ends in the middle direction were vertical, so

the auxiliary deformation could not be achieved by rotation when subjected to uniaxial tension. The effect of this additive deformation decreased with the increase in θ, which resulted in the decrease in equivalent elastic modulus. It was observed that E_1 and E_2 increased with the increase in $\overline{w}$. This was because the increase in filament width would limit the flexibility of its deformation, thus reducing the strain and increasing the equivalent elastic modulus. It is noteworthy that the equivalent elastic moduli (E_1 and E_2) were almost independent of the normalized thickness ($\overline{t}$) but roughly followed a proportional relationship with $\overline{w}$.

Figures 5I(B–D) and 5I(F–H) provide the theoretical and FEA results curves and contour plots of the effective modulus (E_1/E_s) of the second-order fractal metamaterials with different n, where $\overline{w}$ varied from 0.033 to 0.1 and θ varied from 0° to 270° with normalized thickness fixed as 0.067. It was observed that the modulus decreased significantly compared with the first-order structures. For diagonal direction (45°), the impacts of geometry parameters on E_2/E_s can be indicated from curves and contour plots in Figure S8I.

The theoretical prediction of the geometrical impacts on v of the fractal-inspired metamaterials was analyzed, and the results are shown in Figure 5. In the 0° direction, the metamaterials exhibited a wide v tunable domain (−1.1 to 0), and with the increase in θ, the auxetic behavior was gradually weakened, while in the 45° direction, v exhibited a positive value with a narrower domain of 0.2–1.0 and limited impacts resulting from fractal geometry. According to the above analysis, it can be obtained that the tunable critical geometric parameters can be used to achieve adjustable Poisson's ratio of the auxetic materials.

According to Equation 25, Poisson's ratio of metamaterials in the 0° direction was always equal to 0, which was in contradiction to the results of the simulation and experiment results. This mainly resulted from different boundary conditions. In the theoretical model, shearing deformations were allowed when subjected to uniaxial deformations (named boundary condition I), as illustrated in Figure S8II(A). But in experimental and simulation conditions, to limit the shearing deformations, the y-directional deformations were restricted to the boundary nodes, as Figure S8B shows (boundary condition II). The contrast of deformation patterns under boundary conditions I and II is illustrated in Figures S8C–S8E.

Nonlinear mechanical properties under large deformation

The mechanical behavior under large deformation was studied in this section, and due to the mechanical anisotropy of tetra-metamaterials resulting from their 4-fold symmetry geometric construction, two representative directions (0° and 45°) were investigated here. Uniaxial tensile experiments (see details in the supplemental information) and FEA of the metamaterials were carried out (Video S2). Both the first-order and second-order tetra-metamaterials exhibited nonlinear deformations when subjected to uniaxial tensile loads. However, the evolutionary trends of Poisson's ratio (v) and the effective modulus (E_1/E_s and E_2/E_s) varied with the change in deformation mode. These differences in mechanical properties result from the geometrical structural design and the topological arrangement of the filamentary microstructures in the metamaterial units.

The experimental and FEA images and experimental stress-strain (σ-λ) curves in the 0° direction are shown in Figures 6A–6E. It was observed from Figure 6A that the curved filaments were gradually straightened, and as λ increased continuously, the filaments underwent plastic deformation; therefore both first- and second-order

Please cite this article in press as: Li et al., A 4D-printed programmable soft network with fractal design and adjustable hydrophobic performance, Matter (2022), https://doi.org/10.1016/j.matt.2022.12.010

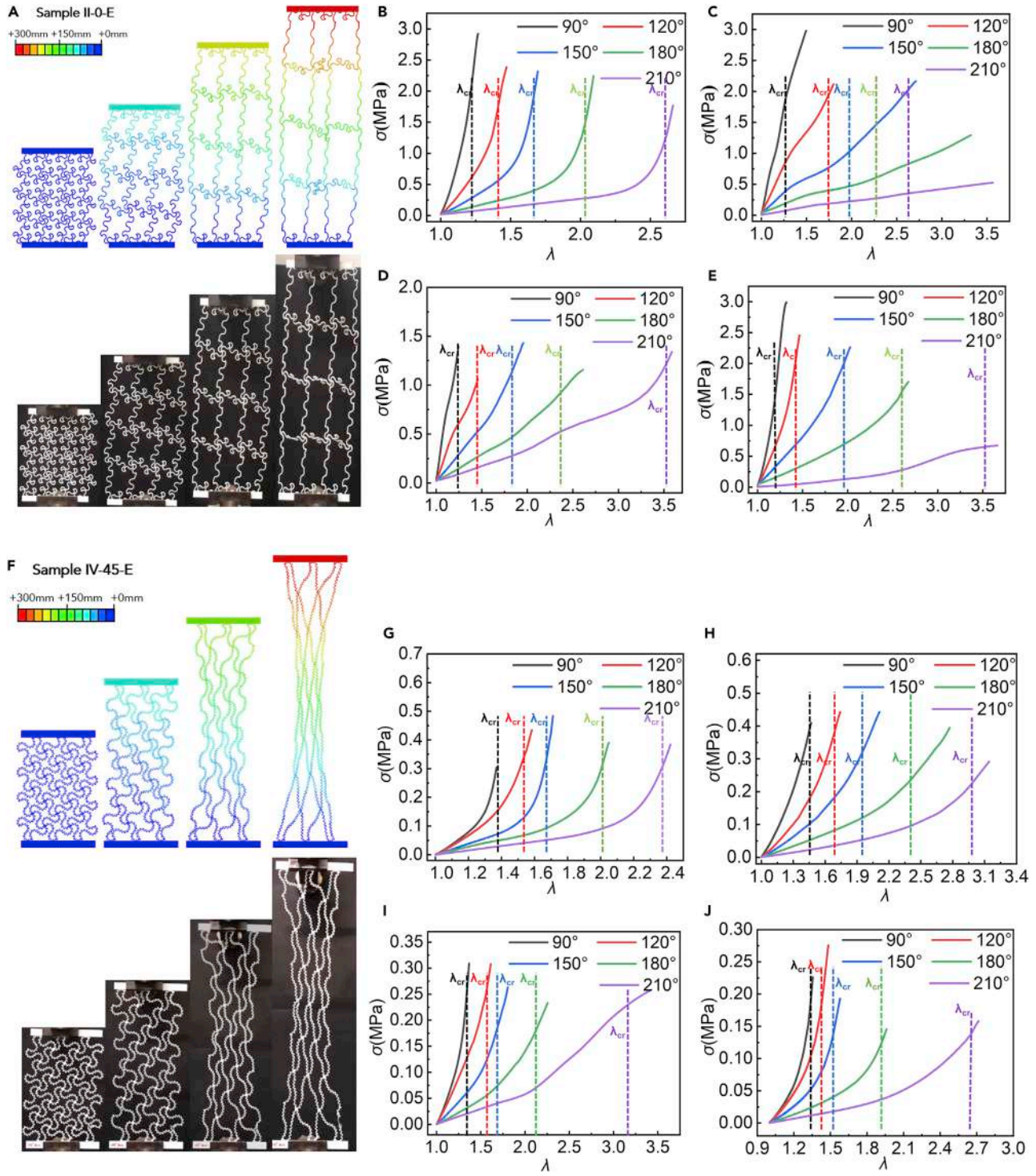

Figure 6. Experiment and finite element analysis results of *v*-λ in 0° and 45° directions

(A) Comparison of experimental optical images and FEM results under different λ of sample II-0-E.

(B–E) *σ*-λ curves in 0° direction of the first-order and second-order structures with n = 2, 4, 6.

(F) Comparison of experimental optical images and FEM results under different λ of sample IV-45-E.

(G–J) *σ*-λ curves in the 45° direction of the first-order and second-order structures with n = 2, 4, 6.

Please cite this article in press as: Li et al., A 4D-printed programmable soft network with fractal design and adjustable hydrophobic performance, Matter (2022), https://doi.org/10.1016/j.matt.2022.12.010

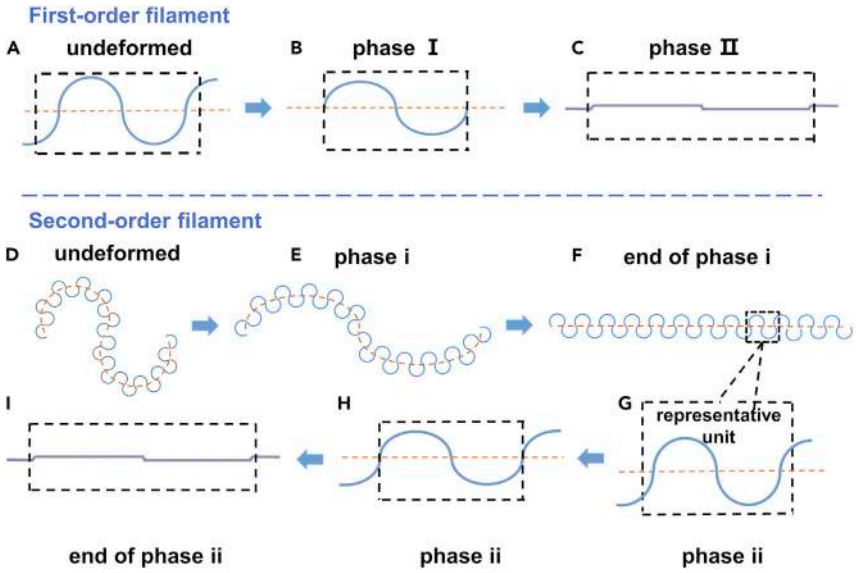

Figure 7. Schematic deformation mode of the first-order and the second-order tetra-metamaterial

(A–C) Schematic deformation mode of the first-order tetra-metamaterials.

(D–I) Schematic multistep deformation mode of the second-order tetra-metamaterials.

metamaterials exhibited nonlinear mechanical behaviors. Figure 6B provides experimental results of σ-λ curves for the first-order metamaterials in the 0° direction with different geometrical parameters. When subjected to uniaxial tensile loads, the first-order structures went through a two-phase deformation model (as shown in Figures 7A–7C), leading to J-shape σ-λ curves. The metamaterials first went through a bending-dominated phase (phase I) at a small strain ($\lambda < \lambda_{cr}$) where curvy filamentary microstructures were gradually uncurled with λ increase. In phase I, σ-λ curves exhibited a relatively low growth as λ increased, signifying low equivalent elastic modulus (E_1/E_s and E_2/E_s), and when curvy filamentary microstructures were stretched to straight, an obvious faster-growing stage was observed as the transitional strain (λ_{tr}) was exceeded. Then the metamaterials entered the stretching-dominated deformation phase (phase II) where E_1 and E_2 were mainly determined by the second moment of the sectional area because the filamentary microstructures were fully stretched to straight. The transition was completed with the critical strain (λ_{cr}) strain exceeded, then the J-shaped σ-λ curve entered the linear hardening stage, and the σ-λ curves exhibited fast growth and high values of equivalent elastic modulus. Both the FEA and the theoretical results indicated that the normalized tangent modulus $E_t(\lambda_{cr})/E_s$ decreased as θ increased, and λ_{cr} increased as θ increased.

Figures 6C–6E provide experimental results of σ-λ curves for the second-order metamaterials in the 0° direction with different n. For the second-order fractal metamaterials in the 0° direction, the deformation mode showed a significant difference from that of the first-order metamaterials, which could be divided into three deformation phases by two critical relative strains (ε_{cr1} and ε_{cr2}), as illustrated in Figures 7D–7I. Phases i and ii were bending dominated. In phase i, first-order morphological structures in second-order structures (as the orange dotted lines denote in Figure 7) were gradually uncurled as λ increased along with slight deformation of the second-order morphological structures (as the blue line denotes in Figure 7). The first-order morphological structures were fully uncurled as λ increased to λ_{cr1}, and in phase ii,

Please cite this article in press as: Li et al., A 4D-printed programmable soft network with fractal design and adjustable hydrophobic performance, Matter (2022), https://doi.org/10.1016/j.matt.2022.12.010

second-order filamentary microstructures were gradually stretched to flat as λ exceeded λ_{cr2}. When λ exceeded λ_{cr2}, structures entered the stretching-dominated phase (phase iii), where equivalent elastic modulus sharply increased because of the loss of deformability of both first-order morphological structures and second-order structures. Experimental and FEA results indicated that the normalized tangent modulus E_{cr1}/E_s and E_{cr2}/E_s decreased as the central angle (θ) increased. And both critical strain λ_{cr1} and critical strain λ_{cr2} increased as the central angle (θ) increased.

It can be observed from Figures 7F–7J that in the diagonal direction, the σ-λ curves of the metamaterials exhibited the same pattern as that of the first-order metamaterials in 0°. This was mainly because shear deformation was allowed during uniaxial tension in the 45° direction. As the data suggested, both E_1 and E_2 decreased and the critical strain (λ_{cr1}) increased as the central angle increased, leading to a lower modulus for the same strain. In addition, because the shear deformation that mainly resulted from the antisymmetric geometry of the filamentary structures was not allowed in 0° stretching, the effective modulus in the 0° direction was larger than that of 45°. Furthermore, the second-order structures had a lower modulus than first-order structures and the stiffness decreased with n increase. Therefore, when θ = 90°, the effective stiffness had the highest value among all the specimens, and with the increase in n, effective stiffness first decreased before increasing, because, although the number of microfilaments increased, the deformation of wavy filaments was limited by width.

The application of fractal geometry design also had an impact on v. The experimental and simulation v-λ curves are shown in Figures 8I(A–D) and 8II(A–D), where the FEA results agree remarkably with the experimental results. The impacts of geometric parameters on v are shown in the contour plots in Figures 8I(E–H) and 8II(E–H). Both the experimental and the FEA results indicated that the fractal-inspired tetra-metamaterials exhibited negative and positive Poisson's ratio when subjected to uniaxial tensile load in the vertical and diagonal directions, respectively. In the vertical direction, the v-λ curves of the first-order structures first went through a plateau, where Poisson's ratio stayed in relatively stable negative values as λ increased. When λ exceeded the critical value (λ_{crp}), Poisson's ratio attained the minimum value and then increased rapidly to zero. This was because the transverse strain (ε_x) of the metamaterials was induced by the rotation at the nodes of the units and the bending deformation of filamentary structures when external loads were applied. Before λ_{crp} was exceeded, ε_x increased faster than the longitudinal strain (ε_y), and as ε_y continued to increase, the growth rate of ε_x was limited by the two factors mentioned above, and ε_x grew slower than ε_y. Therefore, the values of λ_{crp} and v_{max} were used as characterization parameters for structural Poisson's ratio. In the 0° direction, λ_{cr3} increased as θ and n increased, and the v_{max} decreased as θ increased and decreased as n increased. In the 45° direction, Poisson's ratio decreased with θ increase, and for a certain specimen, Poisson's ratio first increased and then decreased as λ increased.

These results demonstrated that the crucial geometric mechanical parameters (N, n, θ, and $\overline{w}$) can be used well to control the mechanical properties of the fractal-inspired tetra-materials. The adjustable domain of Poisson's ratio of fractal-inspired metamaterials in the vertical and diagonal directions was −1.08 to 0 and 0.2 to 1.6, respectively. At room temperature, the elongation of PLA was ≈10% (see details in the supplemental information), and the failure strain of first-order structures in the 0° and 45° directions was 100% and 195%, respectively, and for second-order structures, the failure strain increased to ∼275% and 300% (reaches ≈30 times compared

Please cite this article in press as: Li et al., A 4D-printed programmable soft network with fractal design and adjustable hydrophobic performance, Matter (2022), https://doi.org/10.1016/j.matt.2022.12.010

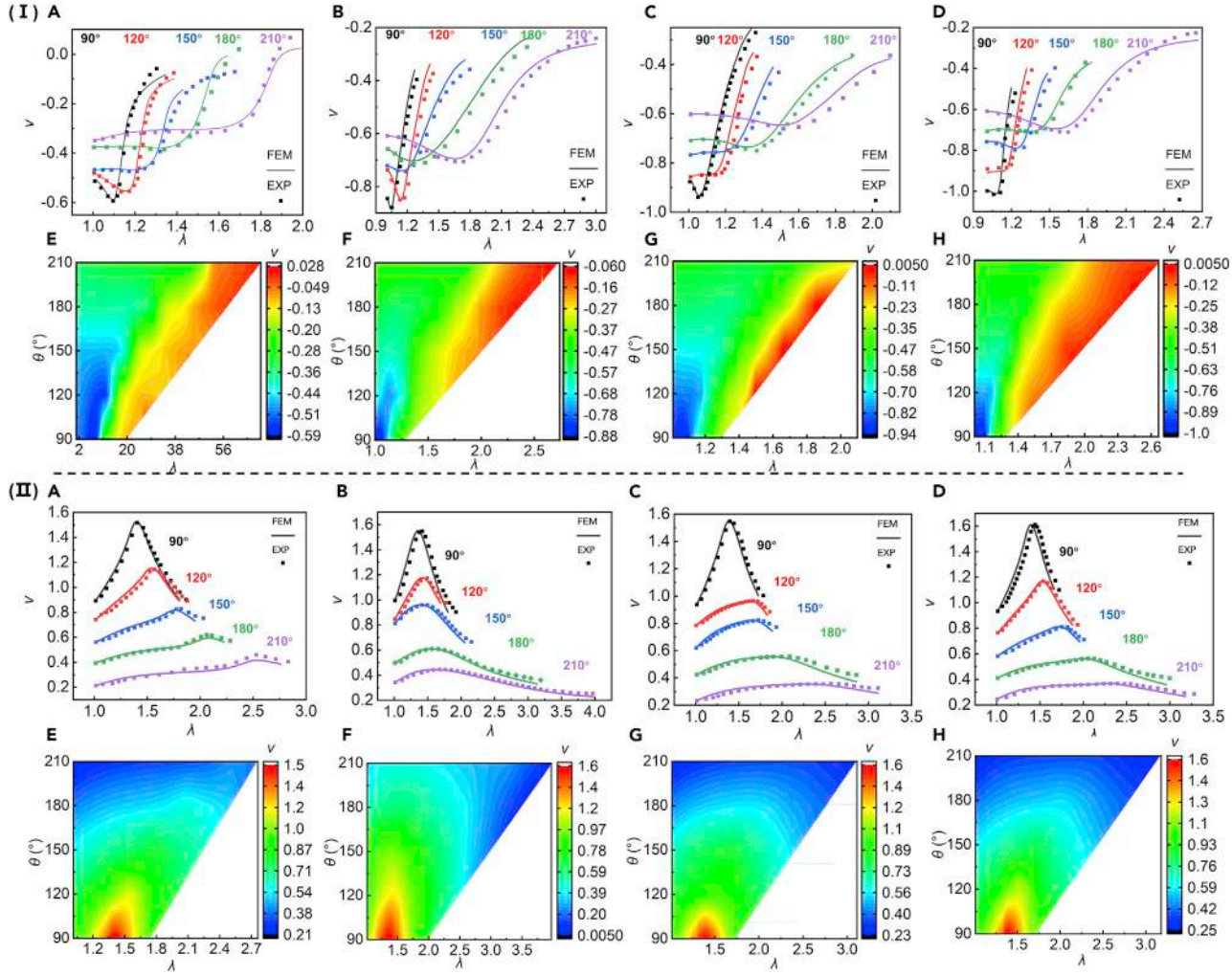

Figure 8. The FEA and experimental results of Poisson's ratio-strain (ν-λ) curves and contour plots in two representative directions

(I) The 0° direction with (A and E) N = 1, (B and F) N = 2, n = 2, (C and G) N = 2, n = 4, and (D and H) N = 2, n = 6.

(II) The 45° direction with (A and E) N = 1, (B and F) N = 2, n = 2, (C and G) N = 2, n = 4, and (D and H) N = 2, n = 6.

with PLA). Therefore, fractal design greatly improved the stretchability and flexibility of metamaterials.

Furthermore, utilizing the SME (Shape Memory Effect) of the PLA materials, the auxetic metamaterials can be programmed into different configurations and recovered to their original shape. The shape memory circle is as shown in Video S1. PLA structures were first put into hot water (80°C) and stretched or twisted into target configurations and then fixed in temporary configurations after cooling and unloading and achieving the mechanical properties of the target structures. Finally, PLA metamaterials recovered their original shape through the reheating process and regained their original mechanical properties.

Sensor characterization

Radial artery pulse signal tests

Radial artery pulse signal tests and characterization of the sensitivity of flexible sensors with different electrodes were obtained and the results are shown in Figure 9. To minimize the impacts on data acquisition by irrelevant factors, the radial artery pulse

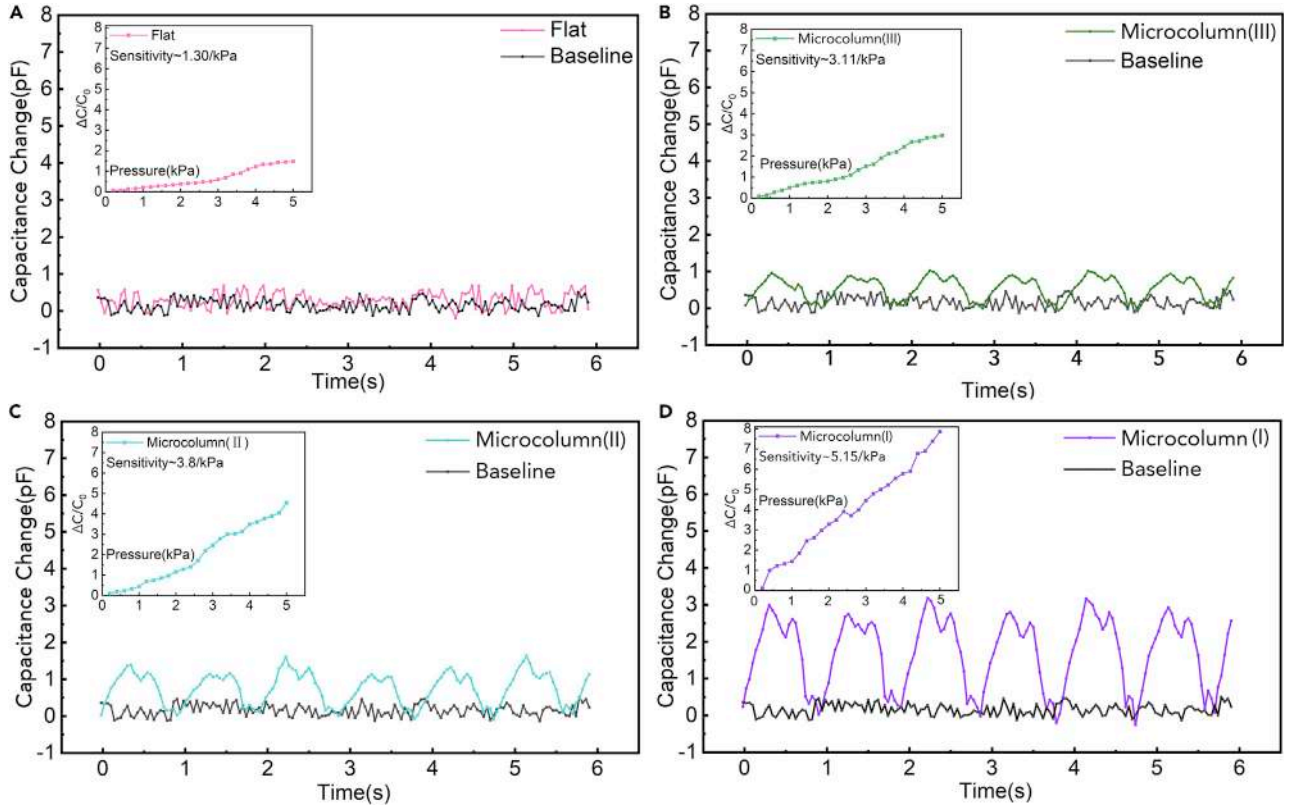

Figure 9. Radial artery pulse and capacitive response waves of flexible sensors with different microcolumn electrodes

(A) Flat electrode.

(B) Electrode with microcolumn III.

(C) Electrode with microcolumn II.

(D) Electrode with microcolumn I.

data were obtained from an identical spot. The results demonstrated that the decreasing column spacing effectively amplified the magnitudes of the retrieved pulse waveforms (Figures 9B–9D). It was noteworthy that the SNR results increased approximately nine times in the waves measured by the film III sensor (SNR ≈ 21.54) compared with the data obtained by the flat electrode (SNR ≈ 2.43), where SNR is defined by the following formula:

$$SNR = avg(\Delta\overline{C_m}) / \sigma_{baseline}. \quad \text{(Equation 27)}$$

Here, $avg(\Delta C_m)$ was defined as the average value of the amplitude in the obtained radial artery pulse waves over test time, and $\sigma_{baseline}$ was defined as the standard deviation of the baseline. The inset images in Figures 9A–9D demonstrate the sensitivity (S) variation with different electrodes, and the results were obtained by using a force gauge (CHB-AHV0; Beijing Long Ding Golden Land Measurement and Control Technology Co., Ltd) with a pressure-sensitive pad and modal shaker (Sinocera Piezotronics, Inc.). Here, ≈2.399, 2.923, and 3.962 times increases in the S were obtained compared with the flat electrodes when the microcolumn spacing of the electrodes decreased from 30 to 10 μm. The S was defined as the relative capacitance change when unit pressure was applied:

$$S = \delta(\Delta C / C_0) / \delta_p, \quad \text{(Equation 28)}$$

where p indicates the applied pressure. Here, it denotes the continuing pressure arising from the radial artery (≈Δ35 mm Hg).[45] The capacitance with and without

Please cite this article in press as: Li et al., A 4D-printed programmable soft network with fractal design and adjustable hydrophobic performance, Matter (2022), https://doi.org/10.1016/j.matt.2022.12.010

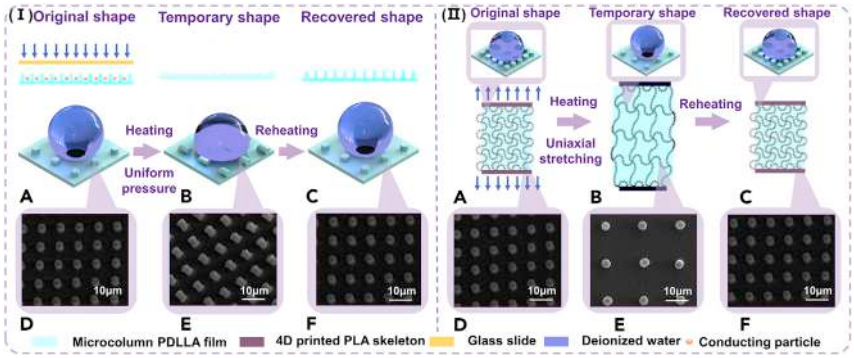

Figure 10. Schematic diagram of the shape memory circle

(I) The out-of-plane and (II) the in-plane shape memory circle of the PLA-based hydrophobic microarrays film: (A) original shape, (B) temporary shape, (C) recovered shape. SEM images of the PLA-based cylindrical microarray film in shape memory cycles: (D) original shape, (E) temporary shape, (F) recovered shape.

applied pressure was set as C and $C_{0,}$ respectively. And the ΔC that represents the radial artery pulse wave was determined by S, as in the following equation:

$$\Delta C = p_{physical} \times C_0 \times S. \quad \text{(Equation 29)}$$

The radial artery pulse waves were obtained by four flexible sensors with electrodes with (1) flat surface and microcolumn structures with spacing of (2) 30 μm, (3) 20 μm, and (4) 10 μm. The inset images in Figure 9 demonstrate the sensitivities of the four devices.

Shape memory characterization

The out-of-plane and in-plane SEM tests were performed with the capacity change (CC) and the static water contact angle (WCA) tested. The trends of S for four flexible sensors with different electrodes (herein referred to as the flat, film I, film II, and film III) were verified by the capacity change and the WCA derived from the pulse pressure signal made by a vibration exciter with the force set as 50 kPa (see the supplemental information for details) and a Theta contact angle analyzer (Biolin Scientific, Sweden), respectively. The out-of-plane SEM cycle tests were performed as shown in Figure 10I. To change the surface microscopic film morphology, a flat glass plate was used to apply a certain pressure (0.2 MPa) to the surface of the samples at 80°C, and the cylindrical microarrays on the surface were deformed. Then the temperature was cooled to room temperature (20°C) and the pressure was removed, then the microscopic morphology of the film surface was fixed to a temporary collapsed shape. Finally, when the samples were reheated to 80°C (above the T_g), the cylindrical microarrays on the samples' surface returned to their original shape (as shown in Figure 10I[A–C]). Figure 10I(D–F) shows the SEM images of microcolumnar SMP arrays with a spacing of 10 μm during the out-of-plane shape memory cycle. It can be observed that columnar structures collapsed and deformed completely after the external force was applied. All the arrays showed collapse and deformation in the same direction on a large area, indicating that the entire surface was uniformly stressed. Figure 10I(D–F) shows the SEM images of the column array in the SEM cycle, and it can be observed that after reheating, the cylindrical microarrays returned to their original shape.

The in-plane SME circle tests were also performed by equiaxial stretching deformation of the films by utilizing the auxetic and SME of the tetra-metamaterials to realize the environmental response of the surface wettability, as illustrated in Figure 10II. The controllable stretching of the structure was realized by utilizing the slide rail

Please cite this article in press as: Li et al., A 4D-printed programmable soft network with fractal design and adjustable hydrophobic performance, Matter (2022), https://doi.org/10.1016/j.matt.2022.12.010

with a calibration tail. Here, films I and II were set as the experimental group, and film III was set as the normal group (see the WCA results of the original state in Figure S8 in supplemental information). The devices were placed in an environmental box at 85°C for 15 min and then quickly stretched to $\lambda = 3$ and $\lambda = 1.5$, respectively (to compare the wettability to that of film III), and then quickly cooled to fix them in their temporary shapes and measure their surface wettability and capacitance change. Subsequently, a lower recovery temperature (60°C) was employed to extend the recovery time of the structures, and the structures were rapidly cooled every 20 s, and then their strain, WCA, and capacitance change were measured. The above steps were repeated until the films recovered to their original shape as shown in Figure 10II(A–F).

The variation of the static WCA and the capacitance change in the out-of-plane and in-plane shape memory circle is illustrated in Figure 11. It can be seen from the histogram in Figure 11A that in the out-of-plane SME test, all the films lost their hydrophobicity after collapsing, with their WCA decreasing to ≈105°. And after recovery, all films regained their original WCA with cylindrical microarrays completely recovered to their original vertical morphology, and film III regained superhydrophobicity. In addition, the capacitance change (as the point plot shows) in the SME circle further indicated the influence of the electrodes' microstructure on the sensitivity of the flexible sensor. Compared with the flat electrodes, the capacity changes of the electrodes with microarrays effectively increased from ∼100 to ∼226, 150, and 125 pF, respectively, when subjected to a uniform pulse pressure of 50 kPa. After collapsing, the capacity change of the sensors decreased to ∼100 pF and recovered to their original value after the shape recovery process. The WCA, capacity change, and strain results in the in-plane SME circles are shown in Figures 11B and 11C. It was observed that the WCA gradually decreased with the capacity change increase to the original value with the shape recovery process of the films. Figure 11D schematically illustrates the variation in the capacitance change in the out-of-plane (bottom graph) and the in-plane (upper graph) SME circle. For the in-plane shape reconfiguration, the sensitivity variation of the sensor was well controlled by the density change of the conductive particles. And for the out-of-plane reconfiguration, the decrease in capacity change was caused by the decrease in the conductive area on the electrodes resulting from the collapsing of the microarray. The above section elaborated on the surface wettability mode and sensitivity conversion of the micrometer-level SMP-based electrodes by regularly controlling the surface morphology of cylindrical microarrays on the film surfaces, and the results indicated that the micrometer-level SMP flexible sensor possessed SME on both macroscopic and micrometer-level scales. And the surface microstructure morphology of the electrodes has a direct impact on the sensitivity of the flexible sensors. Figure 11E shows the pulse signal obtained from the in-plane shape recovery process and Figure 11F shows the average capacity changes obtained from different flexible sensors at original states with gentle or tight attachment. The data were tested five times for each device and averaged.

Conclusion

In summary, this work introduced fractal-designed 4D-printed auxetic metamaterials into health-monitoring sensors and realized their high stretchability, enhanced sensitivity, and adjustable mechanical and electrical properties. A finite-deformation theoretical model was established to serve as a guideline to precisely tune the mechanical properties of auxetic mechanicals through key geometric parameters. And under large deformation, the biomimetic nonlinear mechanical behavior resulting from the transformation from bending- to stretching-dominated phases resulted in

Please cite this article in press as: Li et al., A 4D-printed programmable soft network with fractal design and adjustable hydrophobic performance, Matter (2022), https://doi.org/10.1016/j.matt.2022.12.010

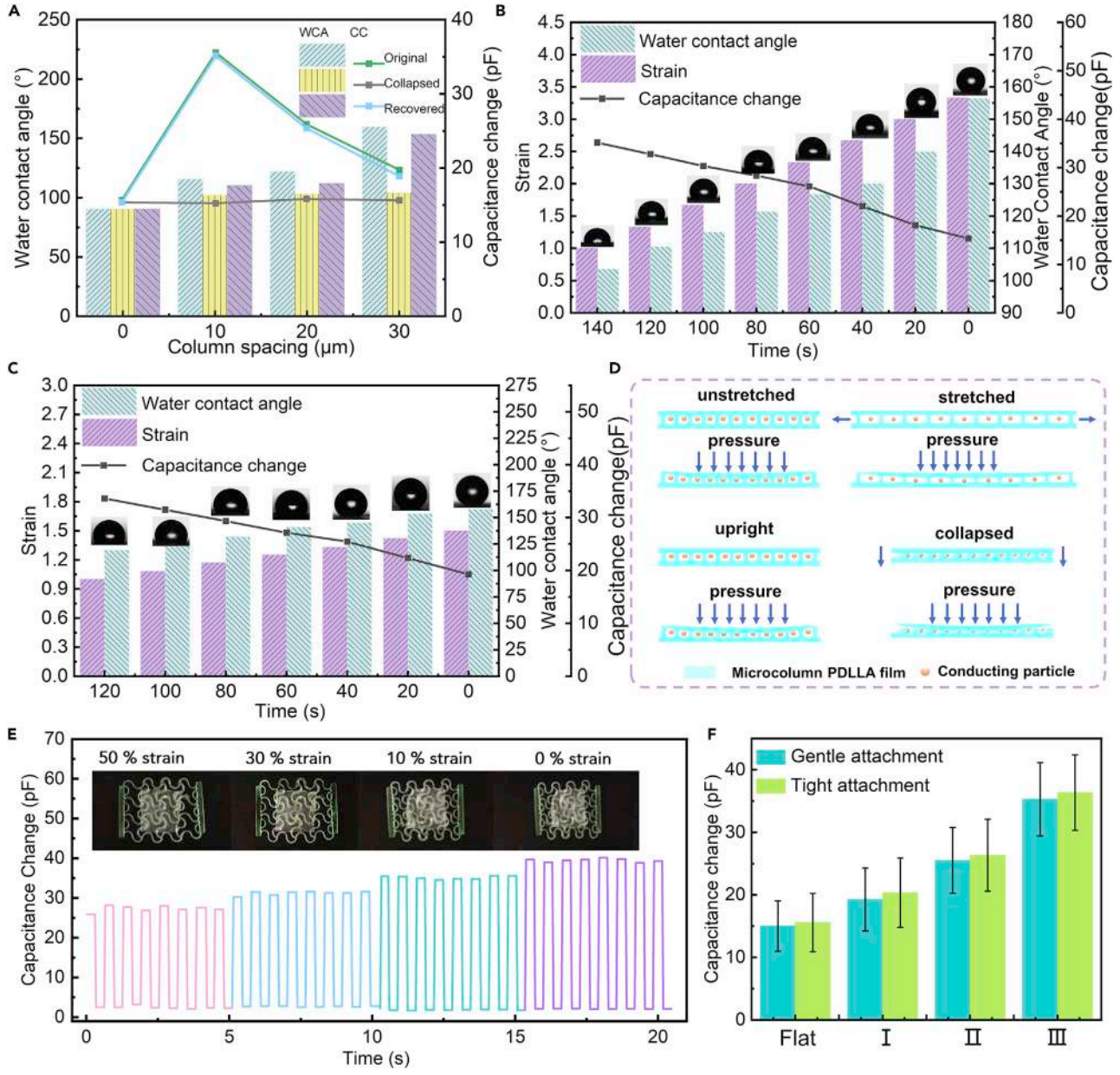

Figure 11. The electrical capability characterization and water contact test results for the shape memory circle

(A) Capacitance change of four flexible sensors.

(B and C) Strain, water contact angle, and capacitance change in the out-of-plane shape memory circle for electrodes with film I and film II, respectively.

(D) Water contact angle and capacitance change in the in-plane shape memory circle.

(E) Capacitance change and optical images in an auxetic deformation shape memory recovery experiment.

(F) Impact of attachment type on the electrical properties of the sensor.

biomimetic J-shape σ-λ curves, indicating its ability to improve the flexibility and compliance in health-monitoring devices. Furthermore, the auxetic metamaterial exhibited a negative Poisson ratio with larger absolute values in a longer effective deformation range than existing works. Finally, its potential in health monitoring was demonstrated by serving as the skeleton in a reconfigurable health sensor with a shape memory biomimetic electrode. The microlevel structures on the electrode surface substantially enhanced the SNR and the sensitivity of the retrieved

Please cite this article in press as: Li et al., A 4D-printed programmable soft network with fractal design and adjustable hydrophobic performance, Matter (2022), https://doi.org/10.1016/j.matt.2022.12.010

signals from the human body. Due to the shape memory effects of both the skeleton and the electrodes and the auxetic mechanical properties of the skeleton, the sensor can be reconfigured with a large-scale temporary shape and realize adjustable mechanical and electrical properties. In brief, the design expands the scope of application and improves the sensibility of the sensor by realizing reconfigurable electrical and mechanical properties.

EXPERIMENTAL PROCEDURES

Resource availability

Lead contact

Further information and requests for resources and reagents should be directed to and will be fulfilled by the lead contact, Jinsong Leng, at lengjs@hit.edu.cn.

Materials availability

This study did not generate new unique reagents.

Data and code availability

All experimental data and source code supporting the findings of this paper are available from the corresponding authors upon reasonable request.

Materials

All reagents were used as received without further purification.

Design and fabrication

The 3D modeling software SOLIDWORKS (3DS Dassault Systèmes, France) was utilized in modeling all the specimens to achieve smooth variation of the filaments' curvatures. Then the models were sliced by the Ultimaker Cura 4.12.1 software. A 3D FDM printer (Mega-x; Shenzhen Anycubic Technology Co., Ltd) was utilized to fabricate all the specimens with PLA filaments as the polymeric material. The printing-bed temperature was set to 80°C to ensure the attachment of the specimen to the building platform, the temperature of the printing nozzle was 200°C, and the moving speed of the printing head was 20 mm/s. The volume of the printed specimens was ~111.55 × 137.00 × 2 mm.

Experimental method

Uniaxial tension experiments were conducted on the printed dumbbell-shaped standard PLA specimens (115 × 65 × 2 mm and a filling density of 100%). The tests were carried out according to the standard ASTM D638 on a Zwick-010 tensile tester with an environmental chamber. The gradient temperatures of 20°C–70°C were selected. Before the experiment was started, each specimen was fixed on the fixture and placed in an environmental chamber at a specified temperature for 15 min to reach thermal equilibrium; the tensile speed in the experiment was set to 2 mm/min until the sample broke.

The stress relaxation experiment of PLA material was carried out at the temperatures of 20°C, 30°C, 40°C, 50°C, 60°C, and 70°C. The test specimen was placed in an environmental chamber at a specified temperature for 15 min. Then, a strain of 1.5% was applied to the test piece at a loading speed of 2 mm/min, and the strain was maintained for 30 min. The attenuation of the force was recorded.

The nonlinear mechanical behavior of the tetra-metamaterial was also obtained by Zwick-010 tensile tester at a tensile rate of 2 mm/min. A Canon HF R806 camera was utilized to record the optical video to calculate Poisson's ratio.

Finite element analysis

The commercial finite element software ABAQUS (3DS Dassault Systèmes, France) was employed to calculate the nonlinear deformation behavior of the metamaterials.

Pulse measurements

The change in local pressure was measured by a Victor VC4091A Precision LCR meter (Victor Instrument Co., Ltd). The sensor was attached to an identical position on the wrist. The capacitance change was put out as a function of time for more than 1 min each time. After measurements, the sensors were removed carefully from the tested area.

Sensitivity and capacitance measurements

The sensitivity (S) and capacitance change measurements were obtained by a custom-built measuring platform containing the Victor VC4091A Precision LCR meter at a frequency of 2 kHz with a 1 V AC signal modal shaker (Sinocera Piezotronics, Inc.) with force gauge (CHB-AHV0; Beijing Long Ding Gold Land Measurement and Control Technology Co., Ltd) that was used to apply pulse loads of 50 kPa at a frequency of 1 Hz to the flexible sensors. The modal shaker was controlled by a power amplifier (YE5872A; Sinocera Piezotronics, Inc.) and a waveform generator (ATF200).

Shape memory and surface wettability test

The WCA tests were carried out in the static state and in the shape memory circle by the Theta contact angle analyzer (Biolin Scientific).

SUPPLEMENTAL INFORMATION

Supplemental information can be found online at https://doi.org/10.1016/j.matt.2022.12.010.

ACKNOWLEDGMENTS

This work was financially supported by the National Natural Science Foundation of China (grants 12072094 and 12172106), Heilongjiang Touyan Innovation Team Program, Fundamental Research Funds for the Central Universities (IR2021106 and IR2021232), Fundamental Research Funds for the Central Universities "0–1 Original exploration plan and the Fundamental Research Funds for the Central Universities" (grant HIT OCEF 2021009). The authors also thank Ms. Yunan Pan and Ms. Chunyan Jiang for their kind help.

AUTHOR CONTRIBUTIONS

Conceptualization, N.L., W.Z., and L.W.L.; investigation, N.L. and W.Z.; experimental design, N.L. and W.Z.; writing – original draft, N.L.; writing – review and editing, W.Z., F.F.L., and L.W.L.; funding acquisition, L.W.L., Y.J.L., and J.S.L.

DECLARATION OF INTERESTS

The authors declare no competing interests.

INCLUSION AND DIVERSITY

We support inclusive, diverse, and equitable conduct of research.

Received: August 26, 2022
Revised: October 10, 2022
Accepted: December 13, 2022
Published: January 10, 2023

REFERENCES

1. McKenzie, R.W., Motta, P.J., and Rohr, J.R. (2014). Comparative squamation of the lateral line canal pores in sharks. J. Fish. Biol. *84*, 1300–1311. https://doi.org/10.1111/jfb.12353.

2. Autumn, K., Liang, Y.A., Hsieh, S.T., Zesch, W., Chan, W.P., Kenny, T.W., Fearing, R., and Full, R.J. (2000). Adhesive force of a single gecko foot-hair. Nature *405*, 681–685. https://doi.org/10.1038/35015073.

3. Gao, H., Wang, X., Yao, H., Gorb, S., and Arzt, E. (2005). Mechanics of hierarchical adhesion structures of geckos. Mech. Mater. *37*, 275–285. https://doi.org/10.1016/j.mechmat.2004.03.008.

4. Gao, X., and Jiang, L. (2004). Water-repellent legs of water striders. Nature *432*, 36. https://doi.org/10.1038/432036a.

5. Guo, Z., and Liu, W. (2007). Biomimic from the superhydrophobic plant leaves in nature: binary structure and unitary structure. Plant Sci. *172*, 1103–1112. https://doi.org/10.1016/j.plantsci.2007.03.005.

6. Cheng, Y.T., and Rodak, D.E. (2005). Is the lotus leaf superhydrophobic? Appl. Phys. Lett. *86*, 144101. https://doi.org/10.1063/1.1895487.

7. Feng, L., Li, S., Li, Y., Li, H., Zhang, L., Zhai, J., Song, Y., Liu, B., Jiang, L., and Zhu, D. (2002). Super-hydrophobic surfaces: from natural to artificial. Adv. Mater. *14*, 1857–1860. https://doi.org/10.1002/adma.200290020.

8. Latthe, S.S., Terashima, C., Nakata, K., and Fujishima, A. (2014). Superhydrophobic surfaces developed by mimicking the hierarchical surface morphology of the lotus leaf. Molecules *19*, 4256–4283. https://doi.org/10.3390/molecules19044256.

9. Luo, Z.Z., Zhang, Z.Z., Hu, L.T., Liu, W.M., Guo, Z.G., Zhang, H.J., and Wang, W.J. (2008). Stable bionic superhydrophobic coating surface fabricated by a conventional curing process. Adv. Mater. *20*, 970–974. https://doi.org/10.1002/adma.200701229.

10. Liu, Y., Tang, J., Wang, R., Lu, H., Li, L., Kong, Y., Qi, K., and Xin, J.H. (2007). Artificial lotus leaf structures from assembling carbon nanotubes and their applications in hydrophobic textiles. J. Mater. Chem. *17*, 1071–1078. https://doi.org/10.1039/b613914k.

11. Pang, C., Koo, J.H., Nguyen, A., Caves, J.M., Kim, M.G., Chortos, A., Kim, K., Wang, P.J., Tok, J.B.H., and Bao, Z. (2015). Highly skin-conformal microhairy sensor for pulse signal amplification. Adv. Mater. *27*, 634–640. https://doi.org/10.1002/adma.201403807.

12. Callens, S.J.P., Arns, C.H., Kuliesh, A., Zadpoor, A.A., and Zadpoor, A.A. (2021). Decoupling minimal surface metamaterial properties through multi-material hyperbolic tilings. Adv. Funct. Mater. *31*, 2101373. https://doi.org/10.1002/adfm.202101373.

13. Yang, C., Boorugu, M., Dopp, A., Ren, J., Martin, R., Han, D., Choi, W., and Lee, H. (2019). 4D printing reconfigurable, deployable and mechanically tunable metamaterials. Mater. Horiz. *6*, 1244–1250. https://doi.org/10.1039/c9mh00302a.

14. Yu, H., Liang, B., Zhao, Z., Liu, P., Lei, H., Song, W., Chen, M., and Guo, X. (2021). Metamaterials with a controllable thermal-mechanical stability: mechanical designs, theoretical predictions and experimental demonstrations. Compos. Sci. Technol. *207*, 108694. https://doi.org/10.1016/j.compscitech.2021.108694.

15. Ni, X., Guo, X., Li, J., Huang, Y., Zhang, Y., and Rogers, J.A. (2019). 2D mechanical metamaterials with widely tunable unusual modes of thermal expansion. Adv. Mater. *31*, 1905405. https://doi.org/10.1002/adma.201905405.

16. Zhao, W., Liu, L., Zhang, F., Leng, J., and Liu, Y. (2019). Shape memory polymers and their composites in biomedical applications. Mater. Sci. Eng. C Mater. Biol. Appl. *97*, 864–883. https://doi.org/10.1016/j.msec.2018.12.054.

17. Dong, J., Ye, G., Wang, Y., Jin, F., and Fan, H. (2021). Design, manufacture and crushing behaviors of buckling-inspired auxetic meta-lattice structures. Int. J. Smart Nano Mater. *12*, 491–510. https://doi.org/10.1080/19475411.2021.1966855.

18. Greaves, G.N., Greer, A.L., Lakes, R.S., and Rouxel, T. (2011). Poisson's ratio and modern materials. Nat. Mater. *10*, 823–837. https://doi.org/10.1038/NMAT3177.

19. Kolken, H.M.A., and Zadpoor, A.A. (2017). Auxetic mechanical metamaterials. RSC Adv. *7*, 5111–5129. https://doi.org/10.1039/c6ra27333e.

20. Babaee, S., Shim, J., Weaver, J.C., Chen, E.R., Patel, N., and Bertoldi, K. (2013). 3D soft metamaterials with negative Poisson' ratio. Adv. Mater. *25*, 5044–5049. https://doi.org/10.1002/adma.201301986.

21. Zhang, F., Wen, N., Wang, L., Bai, Y., and Leng, J. (2021). Design of 4D printed shape-changing tracheal stent and remote controlling actuation. Int. J. Smart Nano Mater. *12*, 375–389. https://doi.org/10.1080/19475411.2021.1974972.

22. Ma, Y., Feng, X., Rogers, J.A., Huang, Y., and Zhang, Y. (2017). Design and application of 'J-shaped' stress-strain behavior in stretchable electronics: a review. Lab Chip *17*, 1689–1704. https://doi.org/10.1039/c7lc00289k.

23. Wang, D., Xu, H., Wang, J., Jiang, C., Zhu, X., Ge, Q., and Gu, G. (2020). Design of 3D printed programmable horseshoe lattice structures based on a phase-evolution model. ACS Appl. Mater. Interfaces *12*, 22146–22156. https://doi.org/10.1021/acsami.0c04097.

24. Xin, X., Liu, L., Liu, Y., and Leng, J. (2020). 4D printing auxetic metamaterials with tunable, programmable, and reconfigurable mechanical properties. Adv. Funct. Mater. *30*, 2004226. https://doi.org/10.1002/adfm.202004226.

25. Jungebluth, P., Haag, J.C., Sjöqvist, S., Gustafsson, Y., Beltrán Rodríguez, A., Del Gaudio, C., Bianco, A., Dehnisch, I., Uhlén, P., Baiguera, S., et al. (2014). Tracheal tissue engineering in rats. Nat. Protoc. *9*, 2164–2179. https://doi.org/10.1038/nprot.2014.149.

26. Ma, Q., and Zhang, Y. (2016). Mechanics of fractal-Inspired horseshoe microstructures for applications in stretchable electronics. ASME. J. Appl. Mech. *83*, 111008. https://doi.org/10.1115/1.4034458.

27. Jang, K.I., Chung, H.U., Xu, S., Lee, C.H., Luan, H., Jeong, J., Cheng, H., Kim, G.T., Han, S.Y., Lee, J.W., et al. (2015). Soft network composite materials with deterministic and bio-inspired designs. Nat. Commun. *6*, 6566. https://doi.org/10.1038/ncomms7566.

28. Ma, Q., Cheng, H., Jang, K.I., Luan, H., Hwang, K.C., Rogers, J.A., Huang, Y., and Zhang, Y. (2016). A nonlinear mechanics model of bio-inspired hierarchical lattice materials consisting of horseshoe microstructures. J. Mech. Phys. Solid. *90*, 179–202. https://doi.org/10.1016/j.jmps.2016.02.012.

29. Van Dillen, T., Onck, P., and Van der Giessen, E. (2008). Models for stiffening in cross-linked biopolymer networks: a comparative study. J. Mech. Phys. Solid. *56*, 2240–2264. https://doi.org/10.1016/j.jmps.2008.01.007.

30. Lu, G.P., Shan, H., Lin, Y., Zhang, K., Zhou, B., Zhong, Q., and Wang, P. (2021). A Fe single atom on N, S-doped carbon catalyst for performing N-alkylation of aromatic amines under solvent-free conditions. J. Mater. Chem. *9*, 25128–25135. https://doi.org/10.1039/d1ta07673f.

31. Tang, L., Wang, L., Yang, X., Feng, Y., Li, Y., and Feng, W. (2021). Poly(N-isopropylacrylamide)-based smart hydrogels: design, properties and applications. Prog. Mater. Sci. *115*, 100702. https://doi.org/10.1016/j.pmatsci.2020.100702.

32. Bertoldi, K., Vitelli, V., Christensen, J., and van Hecke, M. (2017). Flexible mechanical metamaterials. Nat. Rev. Mater. *2*, 17066. https://doi.org/10.1038/natrevmats.2017.66.

33. Zhang, Y., Zhang, F., Yan, Z., Ma, Q., Li, X., Huang, Y., and Rogers, J.A. (2017). Printing, folding and assembly methods for forming 3D mesostructures in advanced materials. Nat. Rev. Mater. *2*, 17019. https://doi.org/10.1038/natrevmats.2017.19.

34. Wang, H., Zhao, Z., Liu, P., and Guo, X. (2022). A soft and stretchable electronics using laser-induced graphene on polyimide/PDMS composite substrate. npj Flex. Electron. *6*, 26. https://doi.org/10.1038/s41528-022-00161-z.

35. Wang, S., Li, M., Wu, J., Kim, D.H., Lu, N., Su, Y., Kang, Z., Huang, Y., and Rogers, J.A. (2012). Mechanics of epidermal electronics. ASME. J. Appl. Mech. *79*, 031022. https://doi.org/10.1115/1.4005963.

36. Wang, L., Qiao, S., Kabiri Ameri, S., Jeong, H., and Lu, N. (2017). A thin elastic membrane conformed to a soft and rough substrate subjected to stretching/compression. ASME. J. Appl. Mech. *84*, 111003. https://doi.org/10.1115/1.4037740.

37. Zhang, B., Li, H., Cheng, J., Ye, H., Sakhaei, A.H., Yuan, C., Rao, P., Zhang, Y.F., Chen, Z., Wang, R., et al. (2021). Mechanically robust and UV-curable shape-memory polymers for digital light processing based 4D printing. Adv.

Mater. *33*, 2101298. https://doi.org/10.1002/adma.202101298.

38. Fan, J.A., Yeo, W.H., Su, Y., Hattori, Y., Lee, W., Jung, S.Y., Zhang, Y., Liu, Z., Cheng, H., Falgout, L., et al. (2014). Fractal design concepts for stretchable electronics. Nat. Commun. *5*, 3266. https://doi.org/10.1038/ncomms4266.

39. Zhai, F., Feng, Y., Li, Z., Xie, Y., Ge, J., Wang, H., Qiu, W., and Feng, W. (2021). 4D-printed untethered self-propelling soft robot with tactile perception: rolling, racing, and exploring. Matter *4*, 3313–3326. https://doi.org/10.1016/j.matt.2021.08.014.

40. Zhao, W., Huang, Z., Liu, L., Wang, W., Leng, J., and Liu, Y. (2022). Bionic design and performance research of tracheal stent based on shape memory polycaprolactone. Compos. Sci. Technol. *229*, 109671. https://doi.org/10.1016/j.compscitech.2022.109671.

41. Zhao, W., Zhang, F., Leng, J., and Liu, Y. (2019). Personalized 4D printing of bioinspired tracheal scaffold concept based on magnetic stimulated shape memory composites. Compos. Sci. Technol. *184*, 107866. https://doi.org/10.1016/j.compscitech.2019.107866.

42. Zhang, Y.F., Li, Z., Li, H., Li, H., Xiong, Y., Zhu, X., Lan, H., and Ge, Q. (2021). Fractal-based stretchable circuits via electric-field-driven microscale 3D printing for localized heating of shape memory polymers in 4D printing. ACS Appl. Mater. Interfaces *13*, 41414–41423. https://doi.org/10.1021/acsami.1c03572.

43. Su, Q., Zou, Q., Li, Y., Chen, Y., Teng, S.Y., Kelleher, J.T., Nith, R., Cheng, P., Li, N., Liu, W., et al. (2021). A stretchable and strain-unperturbed pressure sensor for motion interference-free tactile monitoring on skins. Sci. Adv. *7*, eabi4563. https://doi.org/10.1126/sciadv.abi4563.

44. He, X., Lin, Y., Ding, Y., Abdullah, A.M., Lei, Z., Han, Y., Shi, X., Zhang, W., and Yu, K. (2022). Reshapeable, rehealable and recyclable sensor fabricated by direct ink writing of conductive composites based on covalent adaptable network polymers. Int. J. Extrem. Manuf. *4*, 015301. https://doi.org/10.1088/2631-7990/ac37f2.

45. Pauca, A.L., Wallenhaupt, S.L., Kon, N.D., and Tucker, W.Y. (1992). Dose radial artery pressure accurately reflect aortic pressure. Chest *102*, 1193–1198. https://doi.org/10.1378/chest.102.4.1193.